ACS APPLIED MATERIALS & INTERFACES

www.acsami.org

Research Article

Highly Reversible Chevrel Phase Mo_6Se_8 Cathode with Low Voltage Hysteresis for Rechargeable Aluminum Batteries

Meng Liu, Guocheng Lv,* Hao Liu, Jian Zhang, Tianming Liu, Lingchang Kong, Libing Liao, and Juchen Guo*

Cite This: *ACS Appl. Mater. Interfaces* 2023, 15, 34698−34703

Read Online

ACCESS | Metrics & More | Article Recommendations | Supporting Information

ABSTRACT: Rechargeable aluminum (Al) batteries have attracted considerable interest as potential large-scale energy storage technologies due to the abundance, high theoretical capacity, and high safety of Al. We report here a highly reversible Al-Mo_6Se_8 prototype cell with low discharge−charge hysteresis (approximately 50 mV under 30 mA g^{-1} at 50 °C), ultra-flat discharge plateau, and exceptional cycle stability: the reversible capacity retaining at a steady 77 mA h g^{-1} after more than 1800 cycles. The Al intercalation-extraction mechanism is probed with *ex situ* and *operando* XRD techniques, revealing the reversible intercalation reaction from Mo_6Se_8 to $Al_{4/3}Mo_6Se_8$. The stable electrochemical performance and unambiguous intercalation mechanism of the Al-Mo_6Se_8 system provide an alternative for beyond-lithium battery technologies.

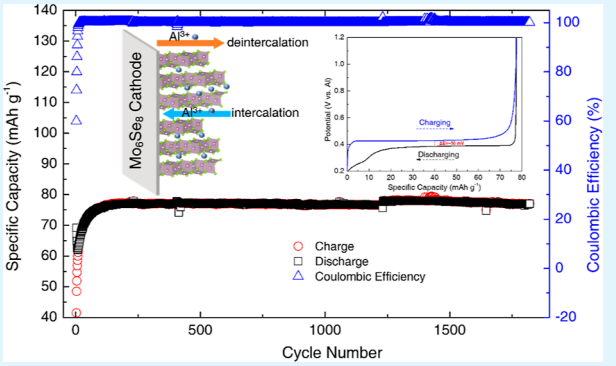

KEYWORDS: *chevrel phase Mo_6Se_8, rechargeable aluminum battery, cycle stability, reversibility, voltage hysteresis*

INTRODUCTION

The reliance on fossil energy results in increasingly severe environmental challenges, including global warming, drought, water pollution, and so forth.[1−3] Rechargeable batteries have the advantage of high energy storage efficiency and, thus, can play an important role to improve energy utilization.[4] Although lithium-ion batteries (LIBs) have achieved successful commercialization, low safety and high cost are challenges prohibiting them from large-scale energy storage applications,[5] for which rechargeable batteries based on multivalent ions are potentially good candidates.[6−8] Rechargeable aluminum batteries (RABs) have received increasing attention due to the abundance, high capacity, and high safety of Al.[9−11] The majority of reported cathode materials for RABs are transition metal oxides and chalcogenides (with the exception of graphite and graphitized carbons),[12−15] which are convenient and rational selections based on their utilizations in LIBs research. Metal oxide and chalcogenide cathodes in RABs mostly follow electrochemical conversion mechanism. The downsides of conversion mechanism include cathode materials disintegration (micro-phase separation), slope-shaped voltage profile without plateaus, and low cycle stability.[16] On the other hand, intercalation-type cathodes typically benefit from stable crystal structure sustaining ion intercalation-extraction, flat voltage plateaus, and excellent cycle stability. To date, the only known Al^{3+} intercalation-type cathode for RABs is Chevrel phase molybdenum sulfide (Mo_6S_8),[17,18] of which the rich interstitial sites and low electronegativity of the sulfide anionic framework enable the facile intercalation of Al^{3+}. Compared to sulfide, selenium (Se) anions have lower electronegativity and higher polarizability, thus in principle, Chevrel phase Mo_6Se_8 may enable faster Al^{3+} ion insertion. Based on this hypothesis, we report Mo_6Se_8 as a cathode material for RABs for the first time. The results indicate that Mo_6Se_8 is a promising cathode material for RABs with low discharge−charge voltage hysteresis (approximately 50 mV under 30 mA g^{-1} at 50 °C), ultra-flat discharge voltage plateau, and excellent cycling stability (retaining 77 mA h g^{-1} for >1800 cycles).

EXPERIMENTAL METHODS

Synthesis of Mo_6Se_8. The ternary Chevrel phase $Cu_2Mo_6Se_8$ was synthesized through solid state reaction by heating stoichiometric mixture of Cu, $MoSe_2$, Mo powders. The mixture was pressed into pellets and heated in a tube furnace. The temperature was ramped up to 1000 °C (5 °C min^{-1}) and held for 24 h and then cooled down to room temperature naturally under hydrogen/argon (5/95 vol %) flow. Subsequently, the prepared $Cu_2Mo_6Se_8$ were dispersed into a 6 M HCl solution and stirred overnight to leach out Cu. After the reaction, the obtained Mo_6Se_8 powders were centrifuged and washed with

Received: March 6, 2023
Accepted: June 20, 2023
Published: July 11, 2023

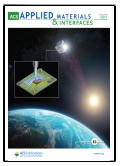

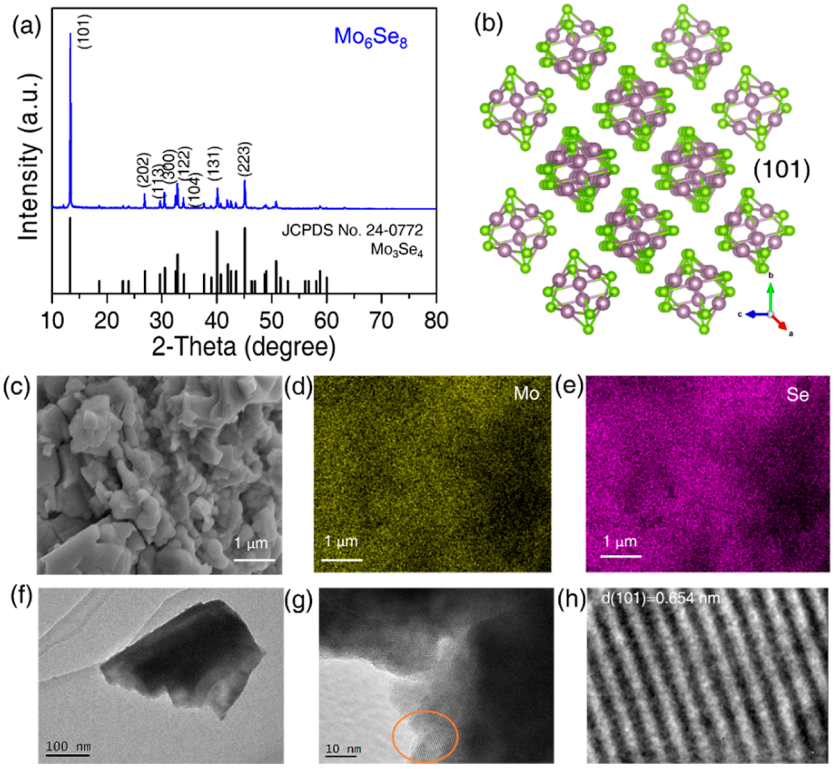

Figure 1. Morphology and micro-structure of Mo_6Se_8: (a) XRD pattern; (b) schematic of the crystal structure from (101) plane; (c–e) SEM image and elemental mapping; (f,g) TEM images at different magnification; and (h) FFT analysis.

deionized water until a neutral pH was reached. The product was dried at 60 °C overnight under vacuum.

Materials Characterization. The crystal structure of Mo_6Se_8 was characterized with powder X-ray diffraction (XRD, Bruker D8) with Cu Kα radiation (λ = 1.5406 Å), 40 kV/40 mA. The morphology of cathodes was characterized with field-emission scanning electron microscopy (SEM, SU8010) and transmission electron microscopy (TEM, JEM). The element analysis of pristine and Al intercalated Mo_6Se_8 with the inductively coupled plasma optical emission spectroscopy (ICP-OES) was performed by Elemental Analysis, Inc. (Lexington, KY).

Electrochemical Analysis. The Al-Mo_6Se_8 batteries were assembled in Swagelok cells (Figure S1 in Supporting Information). Al foil was used as the anode; glass fiber paper GF/D was used as the separator. The cathode was prepared by mixing Mo_6Se_8 powder, carbon black, and polystyrene (as binder) with weight ratio of 8:1:1 in *N*-methylpyrrolidone. The slurry was coated on Mo foil and dried at 60 °C for 12 h under vacuum. The mass loading of Mo_6Se_8 on the cathode is approximately 1 mg cm^{-2}. A chloroaluminate ionic liquid composed of aluminum chloride ($AlCl_3$) and 1-ethyl-3-methylimidazolium chloride ([EMIm]Cl) with a molar ratio of 1.3:1 was used as electrolyte. The Swagelok cells were assembled in an argon-filled glovebox with H_2O and O_2 < 0.01 ppm. The galvanostatic charge–discharge (GCD) tests were performed on a battery tester (LAND CT2001A) at 50 °C with a voltage window of 0.2–1.2 V. Cyclic voltammetry (CV) was carried out using an electrochemical station (CHI760E) in a voltage window from 0.2 to 1.2 V. Potentiostatic discharge method was used to obtain the discharged cathode (Al-intercalated Mo_6Se_8) for ICP-OES analysis by holding the Al-Mo_6Se_8 battery at 0.37 V for 10 h. The discharged Mo_6Se_8 was extracted inside the argon-filled glovebox and washed with adequate amount toluene. *Operando* XRD was performed to probe the crystal structure change during discharge and charge of the Al-Mo_6Se_8 system. The *operando* cell (Figure S2 in Supporting Information) was assembled in an argon-filled glovebox. Carbon paper was used as the current collector with a current density of 30 mA g^{-1}. XRD data were collected with Bruker D8 with Cu Kα radiation (λ = 1.5406 Å), 40 kV/40 mA. The diffraction patterns were recorded by a detector covering a 2θ range from 10 to 55°.

RESULTS AND DISCUSSION

The crystal structure of the synthesized Mo_6Se_8 was characterized using powder XRD (Figure 1a). The sharp diffraction peaks at 2θ = 13.30, 26.91, 30.51, 32.51, 32.84, 40.04, and 45.11° correspond to the (101), (202), (113), (300), (122), (131), and (223) diffraction planes, respectively. All the characteristic peaks are in excellent agreement with the standard card of Mo_6Se_8 (JCPDS Card no. 24-0772).[19] The Rietveld refinement (Figure S3 in Supporting Information) demonstrates excellent fitting of the experimental XRD pattern indicating 98.57% purity of Mo_6Se_8 in the crystalline phase. The energy-dispersive spectroscopy (EDS) shows 49.2 wt % of Mo and 50.8 wt % of Se between these two elements (Figure S3 in Supporting Information). This result agrees well with the elemental analysis from ICP-OES (45.6 wt % of Mo and 50.1 wt % of Se in the entire sample), which is consistent with the formula of Mo_6Se_8. Figure 1b depicts a schematic of the Mo_6Se_8 crystal structure from the (101) plane, which presents a layered framework composed of Mo_6Se_8 clusters. The SEM image and EDS elemental mapping in Figure 1c–e show that the particle size of the pristine Mo_6Se_8 is in the range of 200–1000 nm with uniform distribution of Mo and Se. Lattice fringe from the edge of the bulk particle can be observed in the TEM images (Figure 1f,g). The fast Fourier transform (FFT) analysis exhibits clear reflections with 0.66 nm as displayed in Figure 1h, corresponding to the (101) lattice plane of Mo_6Se_8.

The CV curves of Al-Mo_6Se_8 system were obtained within a voltage window between 0.2 and 1.2 V *versus* Al with a scan rate of 0.1 mV s^{-1} at different temperatures, as temperature is an important parameter for battery performance.[20] As

https://doi.org/10.1021/acsami.3c03231
ACS Appl. Mater. Interfaces 2023, 15, 34698–34703

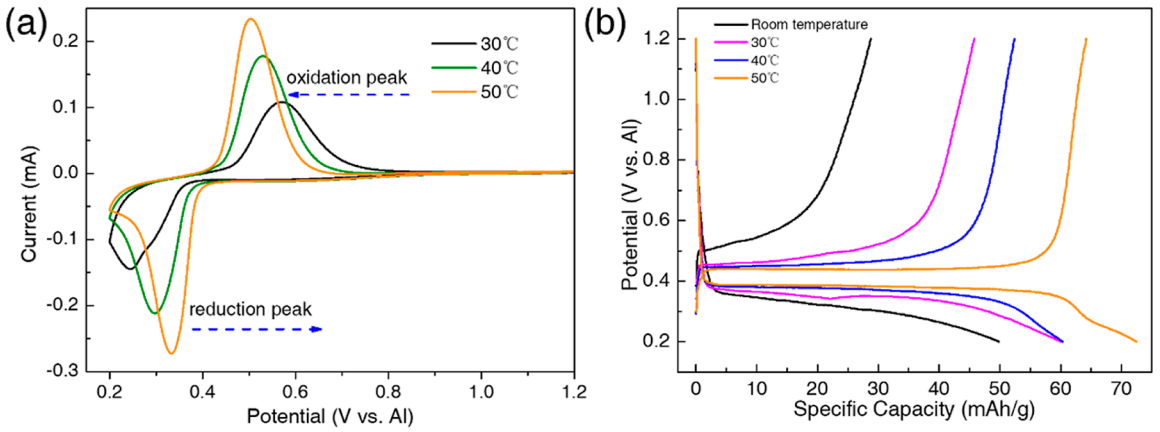

Figure 2. (a) CV curves with a scan rate of 0.1 mV s^{-1} and (b) GCD profiles under 30 mA g^{-1} of Al-Mo_6Se_8 cells at different temperatures.

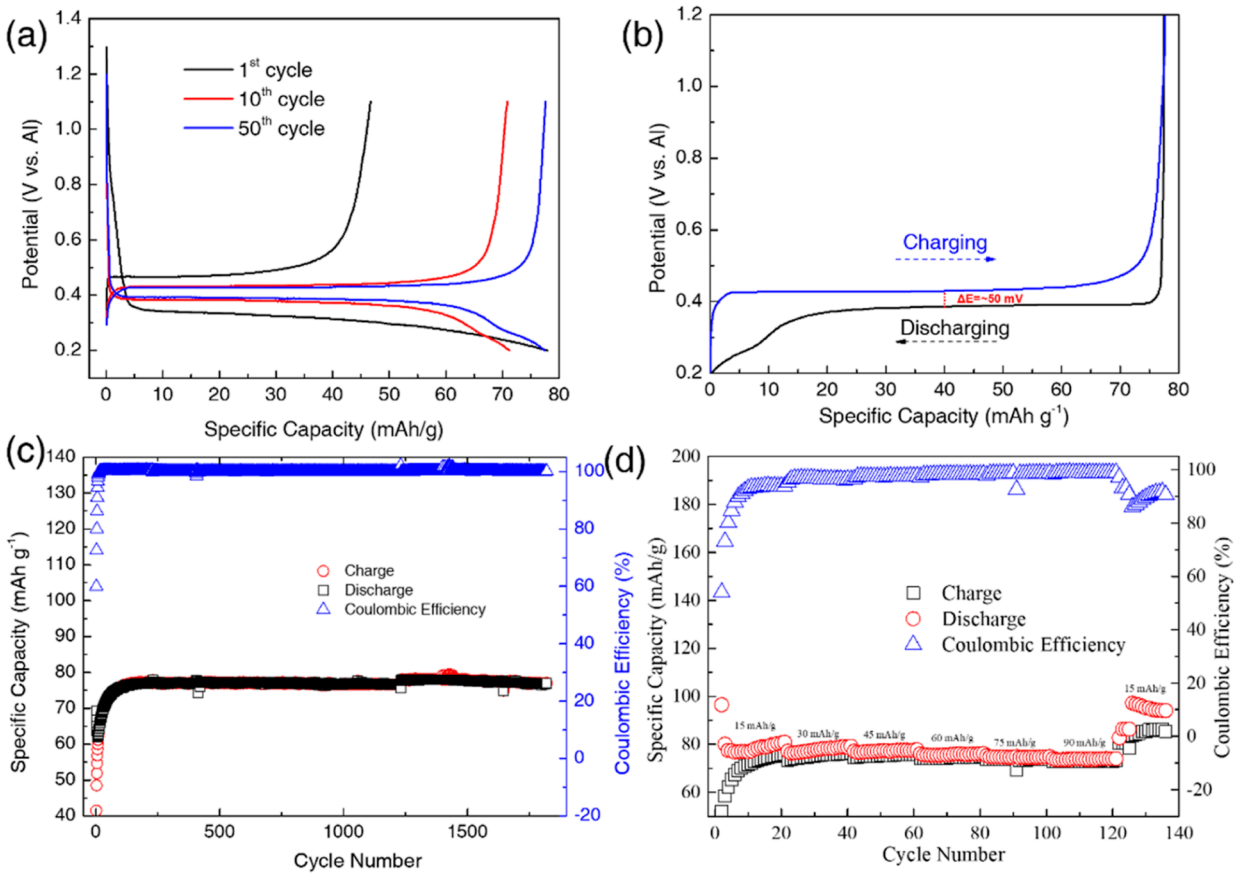

Figure 3. Electrochemical performance of Mo_6Se_8: (a) GCD profiles of the Al-Mo_6Se_8 battery at representative cycles at 30 mA g^{-1}; (b) discharge and charge profiles of Al-Mo_6Se_8 at the 50th cycle; (c) specific discharge capacity and CE vs cycle number at 30 mA g^{-1}; and (d) rate capacity at different current ranging from 15 to 90 mA g^{-1}. All tests are at 50 °C.

displayed in Figure 2a, higher temperature leads to lower voltage polarization of the redox peaks in CV. The anodic peak shifts to lower potential and the cathodic peak shifts to higher potential with increasing temperature. The peak current also increases with increasing temperature, indicating faster reaction kinetics.[21] Multiple CV cycles at room temperature can be found in Figure S4 in Supporting Information. The GCD profiles at different temperatures in Figure 2b demonstrate the same trend as the CV curves, therefore, the remaining electrochemical tests are all performed at 50 °C to achieve higher specific capacity and reduced voltage hysteresis.

Figure 3a shows the voltage profiles of the 1st, 10th, and 50th GCD cycles at 50 °C. In the 1st cycle, a discharge capacity of 78 mA h g^{-1} was achieved (88.6% of the theoretical capacity corresponding to a 4-electron transfer).[22] In the 1800th cycle, the discharge and charge capacity is 77 mA h g^{-1}, and a 100% Coulombic efficiency (CE) is achieved. The voltage profiles of the 10th and 50th cycles exhibit reduced discharge−charge voltage hysteresis compared to the 1st cycle. The GCD profile of the 50th cycle is replotted in Figure 3b, which displays a very low voltage hysteresis of approximately 50 mV and a highly reversible electrochemical profile with

https://doi.org/10.1021/acsami.3c03231
ACS Appl. Mater. Interfaces 2023, 15, 34698−34703

well-defined plateaus in the discharging and charging processes. The long-term cycling result in Figure 3c clearly demonstrates stable capacity retention at 77 mA h g^{-1} and 100% CE after 1800 cycles. The predicted maximum charge transfer to Mo_6Se_8 is $4e^-/Mo_6Se_8$, resulting in the maximal Al intercalated format of $Al_{4/3}Mo_6Se_8$.[22] Elemental analysis through ICP-OES indicates that the discharged Mo_6Se_8 cathode at 0.37 V is composed of 50.15 wt % of Se, 3.16 wt % of Al, and 46.69 wt % of Mo, corresponding to a molecular formula of $Al_{1.39}Mo_6Se_{7.83}$, which agrees well with the predicted $Al_{4/3}Mo_6Se_8$. Therefore, the discharge−charge reactions for Al-Mo_6Se_8 RABs is proposed as follows:

$$4Al + 28AlCl_4^- \leftrightarrow 16Al_2Cl_7^- + 12e^- \quad (1)$$

$$12e^- + 16Al_2Cl_7^- + 3Mo_6Se_8 \leftrightarrow 3Al_{4/3}Mo_6Se_8 + 28AlCl_4^- \quad (2)$$

Figure 3d shows the rate performance of the Al-Mo_6Se_8 battery. When the current density is increased from 15 to 90 mA g^{-1}, the specific capacity decreases slightly. The Al-Mo_6Se_8 cell still delivers approximately 70 mA h g^{-1} capacity at 90 mA g^{-1} current density. The discharge capacity is recovered when the rate reduced back to the original value. The discharge-change voltage hysteresis of Mo_6Se_8 was tested under different current (Figure S5 and Table S1 in Supporting Information). The voltage hysteresis only slightly increases from 53.3 to 68.8 mV when the current is increased from 15 to 90 mA g^{-1}, which is significantly lower than that of most cathodes in RABs. This result indicates that the highly reversible capacity, cycle stability, and low voltage hysteresis of the Al-Mo_6Se_8 battery are among the best RABs (Table S2 in Supporting Information).

To examine the crystal structure change of Mo_6Se_8 during the electrochemical process, *operando* XRD was performed during the first galvanostatic discharge−charge cycle between 1.2 and 0.2 V. As shown in Figure 4a, when discharged from open circuit voltage to 0.2 V, the intensity of the peaks at 13.5, 32.6, 33.0, 34.0, 40.2, 45.2, and 50.9°, which are corresponding to the planes of (101), (300), (122), (104), (131), (223), and (232) gradually decrease, which may be attributed to the lattice disordering in these orientations. Simultaneously, new peaks at 30, 40.5, and 46.7° appear and the origin of these peaks are still under investigation. The crystal structure in the subsequent charge process seems reversed back to the original state: The intensity of the diffraction peaks of the (101), (300), (122), (104), (131), (223), (042), and (232) planes of Mo_6Se_8 gradually reappear as the charge state is increasing, indicating that the material undergoes reversible phase transition during the first discharge and charge process. Figure 4b presents the contour plots of the *operando* XRD patterns of the Mo_6Se_8 electrode at different discharge and charge time. It is noted that the red color represents the high intensity and the blue color represents the low intensity. Between 90 min (discharged to 0.3 V) and 200 min (charged to 0.5 V), the peaks are quite inconspicuous, the poor crystallinity of cathode at lower potential is still a challenge to index the peaks. Nevertheless, the *operando* XRD demonstrates the reversible change of crystal structure of Mo_6Se_8 during Al intercalation and extraction, proving the high reversibility of the Al-Mo_6Se_8 battery.

To confirm the stability of the Mo_6Se_8 cathode after cycling and the effect of long-term cycling on the crystal structure, XRD pattern of the Mo_6Se_8 cathode was obtained after

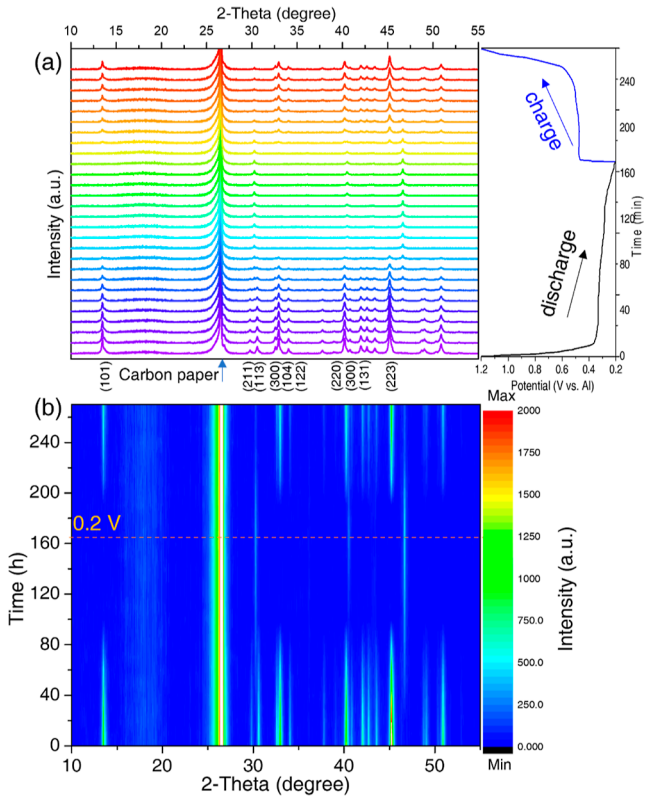

Figure 4. (a) *Operando* XRD patterns and (b) contour plots of *operando* XRD of Mo_6Se_8 in the first galvanostatic discharge−charge cycle *vs* Al.

different discharge−charge cycles. As shown in Figure 5, the XRD peaks of the Mo_6Se_8 cathode remain sharp after 50

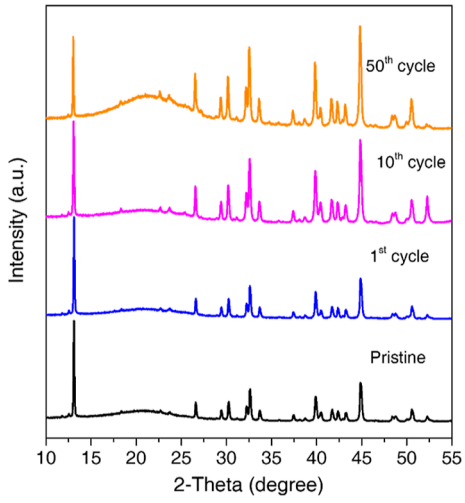

Figure 5. XRD patterns of the Mo_6Se_8 cathode after different cycles.

cycles. This confirms that the crystal structure of Mo_6Se_8 sustains repeated Al intercalation-extraction during cycling. Interestingly, the peak at 13.5° corresponding to the (101) plan becomes less intensive during cycling using the rest of XRD peaks as the reference, indicating the increased disordering of (101) plan due to repeated Al intercalation and extraction.

https://doi.org/10.1021/acsami.3c03231
ACS Appl. Mater. Interfaces 2023, 15, 34698−34703

CONCLUSIONS

Mo_6Se_8 is synthesized in this study *via* high-temperature solid-phase sintering. The obtained Mo_6Se_8 is found to be promising as a RAB cathode material, which may be suitable for land-based, grid-scale electrical energy storage applications. The RABs with Mo_6Se_8 cathode and Al anode exhibit excellent performances, including retaining a reversible specific discharge capacity of 77 mA h g^{-1} at 30 mA g^{-1} for >1800 cycles. Moreover, the Al-Mo_6Se_8 batteries operate with very low voltage hysteresis (~50 mV under 30 mA g^{-1} at 50 °C) and an ultra-flat discharge platform. The crystal structure of Mo_6Se_8 appears to experience reversible phase transition during Al intercalation and extraction. It also appears that the crystallinity at certain planes is decreased due to repeated Al insertion. The details and the origin of the crystal structure change will be investigated in our following study.

ASSOCIATED CONTENT

Supporting Information

The Supporting Information is available free of charge at https://pubs.acs.org/doi/10.1021/acsami.3c03231.

Images of Swagelok cell; operando XRD experiment setup, XRD structure refinement results and EDS mapping results of Mo_6Se_8; CV curve of Al-Mo_6Se_8 battery at room temperature with scan rate of 0.1 mV s^{-1}; the charging and discharging profiles of Mo_6Se_8 at different current densities; table of specific capacity and voltage hysteresis of cathode at different current densities; and table of comparison of the electrochemical performance of different RAB cathodes (PDF)

AUTHOR INFORMATION

Corresponding Authors

Guocheng Lv − *Engineering Research Center of Ministry of Education for Geological Carbon Storage and Low Carbon Utilization of Resources, Beijing Key Laboratory of Materials Utilization of Nonmetallic Minerals and Solid Wastes, National Laboratory of Mineral Materials, School of Materials Science and Technology, China University of Geosciences, Beijing 100083, China;* orcid.org/0000-0002-3719-8431; Email: guochenglv@cugb.edu.cn

Juchen Guo − *Materials Science and Engineering Program and Department of Chemical and Environmental Engineering, University of California—Riverside, Riverside, California 92521, United States;* orcid.org/0000-0001-9829-1202; Email: jguo@engr.ucr.edu

Authors

Meng Liu − *Engineering Research Center of Ministry of Education for Geological Carbon Storage and Low Carbon Utilization of Resources, Beijing Key Laboratory of Materials Utilization of Nonmetallic Minerals and Solid Wastes, National Laboratory of Mineral Materials, School of Materials Science and Technology, China University of Geosciences, Beijing 100083, China*

Hao Liu − *School of Science, China University of Geosciences Beijing, Beijing 100083, China*

Jian Zhang − *Materials Science and Engineering Program, University of California—Riverside, Riverside, California 92521, United States;* orcid.org/0000-0003-0356-7611

Tianming Liu − *School of Science, China University of Geosciences Beijing, Beijing 100083, China*

Lingchang Kong − *Engineering Research Center of Ministry of Education for Geological Carbon Storage and Low Carbon Utilization of Resources, Beijing Key Laboratory of Materials Utilization of Nonmetallic Minerals and Solid Wastes, National Laboratory of Mineral Materials, School of Materials Science and Technology, China University of Geosciences, Beijing 100083, China*

Libing Liao − *Engineering Research Center of Ministry of Education for Geological Carbon Storage and Low Carbon Utilization of Resources, Beijing Key Laboratory of Materials Utilization of Nonmetallic Minerals and Solid Wastes, National Laboratory of Mineral Materials, School of Materials Science and Technology, China University of Geosciences, Beijing 100083, China;* orcid.org/0000-0001-5312-8487

Complete contact information is available at: https://pubs.acs.org/10.1021/acsami.3c03231

Notes

The authors declare no competing financial interest.

ACKNOWLEDGMENTS

This work was supported by the National Natural Science Foundation of China (no. 21875223). J.Z. and J.G. acknowledge the support from U.S. National Science Foundation through grant CBET-1751929.

REFERENCES

(1) Liu, H.; Xie, R.; Luo, Y.; Cui, Z.; Yu, Q.; Gao, Z.; Zhang, Z.; Yang, F.; Kang, X.; Ge, S.; Li, S.; Gao, X.; Chai, G.; Liu, L.; Liu, B. Dual Interfacial Engineering of a Chevrel Phase Electrode Material for Stable Hydrogen Evolution at 2500 mA cm^{-2}. *Nat. Commun.* **2022**, *13*, 6382.

(2) Chen, C.; Yan, X.; Wu, Y.; Liu, S.; Zhang, X.; Sun, X.; Zhu, Q.; Wu, H.; Han, B. Boosting the Productivity of Electrochemical CO_2 Reduction to Multi-Carbon Products by Enhancing CO_2 Diffusion through a Porous Organic Cage. *Angew. Chem., Int. Ed.* **2022**, *61*, No. e202202607.

(3) Verma, V.; Kumar, S.; Manalastas, W., Jr.; Satish, R.; Srinivasan, M. Progress in Rechargeable Aqueous Zinc- and Aluminum-Ion Battery Electrodes: Challenges and Outlook. *Adv. Sustainable Syst.* **2019**, *3*, 1800111.

(4) Jeong, G.; Kim, Y. U.; Kim, H.; Kim, Y. J.; Sohn, H. J. Prospective Materials and Applications for Li Secondary Batteries. *Energy Environ. Sci.* **2011**, *4*, 1986−2002.

(5) Li, C.; Wu, J.; Ma, F.; Chen, Y.; Fu, L.; Zhu, Y.; Zhang, Y.; Wang, P.; Wu, Y.; Huang, W. High-Rate and High-Voltage Aqueous Rechargeable Zinc Ammonium Hybrid Battery from Selective Cation Intercalation Cathode. *ACS Appl. Energy Mater.* **2019**, *2*, 6984−6989.

(6) Zhou, Q.; Wang, D.; Ni, L.; Zhang, H.; Zhao, J. Willow Leaf-shape $ReSe_2$@ C as Positive Electrode Material for Aluminum-Ion Batteries. *J. Alloys Compd.* **2022**, *909*, 164773.

(7) Li, T.; Hu, H.; Cai, T.; Liu, X.; Zhang, Y.; Zhao, L.; Xing, W.; Yan, Z. Ultrafast and Long-Cycle Stable Aluminum Polyphenylene Batteries. *ACS Appl. Mater. Interfaces* **2022**, *14*, 30927−30936.

(8) Ejigu, A.; Le Fevre, L. W.; Elgendy, A.; Spencer, B. F.; Bawn, C.; Dryfe, R. A. W. Optimization of Electrolytes for High-Performance Aqueous Aluminum-Ion Batteries. *ACS Appl. Mater. Interfaces* **2022**, *14*, 25232−25245.

(9) Kravchyk, K. V.; Kovalenko, M. V. The Pitfalls in Nonaqueous Electrochemistry of Al-Ion and Al Dual-Ion Batteries. *Adv. Energy Mater.* **2020**, *10*, 2002151.

(10) Wu, F.; Yang, H.; Bai, Y.; Wu, C. Paving the Path toward Reliable Cathode Materials for Aluminum-Ion Batteries. *Adv. Mater.* **2019**, *31*, 1806510.

(11) Lin, M. C.; Gong, M.; Lu, B.; Wu, Y.; Wang, D. Y.; Guan, M.; Angell, M.; Chen, C.; Yang, J.; Hwang, B. J.; Dai, H. An Ultrafast Rechargeable Aluminium-Ion Battery. *Nature* **2015**, *520*, 324−328.
(12) Sun, H.; Wang, W.; Yu, Z.; Yuan, Y.; Wang, S.; Jiao, S. A New Aluminium-Ion Battery with High Voltage, High Safety and Low Cost. *Chem. Commun.* **2015**, *51*, 11892−11895.
(13) Zhang, Y.; Zhang, B.; Li, J.; Liu, J.; Huo, X.; Kang, F. SnSe Nano-Particles as Advanced Positive Electrode Materials for Rechargeable Aluminum-Ion Batteries. *Chem. Eng. J.* **2021**, *403*, 126377.
(14) Jiang, J.; Li, H.; Fu, T.; Hwang, B. J.; Li, X.; Zhao, J. One-Dimensional $Cu_{2-x}Se$ Nanorods as the Cathode Material for High-Performance Aluminum-Ion Battery. *ACS Appl. Mater. Interfaces* **2018**, *10*, 17942−17949.
(15) Tan, B.; Lu, T.; Luo, W.; Chao, Z.; Dong, R.; Fan, J. A novel MoS_2-MXene Composite Cathode for Aluminum-Ion Batteries. *Energy Fuel.* **2021**, *35*, 12666−12670.
(16) Levi, E.; Gershinsky, G.; Aurbach, D.; Isnard, O. Crystallography of Chevrel Phases, MMo_6T_8 (M= Cd, Na, Mn, and Zn, T= S, Se) and Their Cation Mobility. *Inorg. Chem.* **2009**, *48*, 8751−8758.
(17) Geng, L.; Lv, G.; Xing, X.; Guo, J. Reversible Electrochemical Intercalation of Aluminum in Mo_6S_8. *Chem. Mater.* **2015**, *27*, 4926−4929.
(18) Geng, L.; Scheifers, J.; Zhang, J.; Bozhilov, K. N.; Fokwa, B. P. T.; Guo, J. Crystal Structure Transformation in Chevrel Phase Mo_6S_8 Induced by Aluminum Intercalation. *Chem. Mater.* **2018**, *30*, 8420−8425.
(19) Saha, P.; Jampani, P. H.; Datta, M. K.; Hong, D.; Gattu, B.; Patel, P.; Kadakia, K. S.; Manivannan, A.; Kumta, P. N. A Rapid Solid-State Synthesis of Electrochemically Active Chevrel Phases (Mo_6T_8; T=S, Se) for Rechargeable Magnesium Batteries. *Nano Res.* **2017**, *10*, 4415−4435.
(20) Badrinarayanan, R.; Zhao, J.; Tseng, K. J.; Skyllas-Kazacos, M. Extended Dynamic Model for Ion Diffusion in All-vanadium Redox Flow Battery Including the Effects of Temperature and Bulk Electrolyte Transfer. *J. Power Sources* **2014**, *270*, 576−586.
(21) Kitada, A.; Nakamura, K.; Fukami, K.; Murase, K. Electrochemically Active Species in Aluminum Electrodeposition Baths of $AlCl_3$/Glyme Solutions. *Electrochim. Acta* **2016**, *211*, 561−567.
(22) Gocke, E.; Schoellhorn, R.; Aselmann, G.; Mueller-Warmuth, W. Molybdenum Cluster Chalcogenides Mo_6X_8: Intercalation of Lithium via Electron/Ion Transfer. *Inorg. Chem.* **1987**, *26*, 1805−1812.

https://doi.org/10.1021/acsami.3c03231
ACS Appl. Mater. Interfaces 2023, 15, 34698−34703